

# Construction and Commissioning of Mid-Infrared SASE FEL at cERL

Yosuke Honda<sup>a</sup>, Masahiro Adachi<sup>a</sup>, Shu Eguchi<sup>a</sup>, Masafumi Fukuda<sup>a</sup>, Ryoichi Hajima<sup>c</sup>, Nao Higashi<sup>a</sup>, Masayuki Kakehata<sup>b</sup>, Ryukou Kato<sup>a</sup>, Takako Miura<sup>a</sup>, Tsukasa Miyajima<sup>a</sup>, Shinya Nagahashi<sup>a</sup>, Norio Nakamura<sup>a</sup>, Kazuyuki Nigorikawa<sup>a</sup>, Takashi Nogami<sup>a</sup>, Takashi Obina<sup>a</sup>, Hidenori Sagehashi<sup>a</sup>, Hiroshi Sakai<sup>a</sup>, Tadatake Sato<sup>b</sup>, Miho Shimada<sup>a</sup>, Tatsuro Shioya<sup>a</sup>, Ryota Takai<sup>a</sup>, Olga Tanaka<sup>a</sup>, Yasunori Tanimoto<sup>a</sup>, Kimichika Tsuchiya<sup>a</sup>, Takashi Uchiyama<sup>a</sup>, Akira Ueda<sup>a</sup>, Masahiro Yamamoto<sup>a</sup>, Hidehiko Yashiro<sup>b</sup>, Demin Zhou<sup>a</sup>

<sup>a</sup>High Energy Accelerator Research Organization (KEK), 1-1 Oho, Tsukuba, Ibaraki 305-0801, Japan

<sup>b</sup>National Institute of Advanced Industrial Science and Technology (AIST), Central 2, 1-1-1 Umezono, Tsukuba, 305-8568, Japan

<sup>c</sup>National Institutes for Quantum and Radiological Science and Technology (QST), Tokai, Ibaraki 3191106, Japan

---

## Abstract

The mid-infrared range is an important spectrum range where materials exhibit a characteristic response corresponding to their molecular structure. A free-electron laser (FEL) is a promising candidate for a high-power light source with wavelength tunability to investigate the nonlinear response of materials. Although the self-amplification spontaneous emission (SASE) scheme is not usually adopted in the mid-infrared wavelength range, it may have advantages such as layout simplicity, the possibility of producing a single pulse, and scalability to a short-wavelength facility. To demonstrate the operation of a mid-infrared SASE FEL system in an energy recovery linac (ERL) layout, we constructed an SASE FEL setup in cERL, a test facility of the superconducting linac with the ERL configuration. Despite the adverse circumstance of space charge effects due to the given boundary condition of the facility, we successfully established the beam condition at the undulators, and observed FEL emission at a wavelength of 20  $\mu\text{m}$ . The results show that the layout of cERL has the potential for serving as a mid-infrared light source.

---

## 1. INTRODUCTION

Human society depends on various materials, which are being further developed by game-changing innovations in the production of useful materials. One of the most fundamental properties of a material is its response to electromagnetic radiation. In particular, in the mid-infrared spectrum range, which is defined as 3-50  $\mu\text{m}$  in wavelength, materials exhibit a characteristic response corresponding to their molecular structure. By irradiating a narrow-band mid-infrared radiation that targets one of the oscillation modes of a material, we can selectively excite the mode in a thermally non-equilibrium way. It will be useful for efficiently converting one material to another or for realizing a new state of material that cannot be achieved by using a conventional method [1, 2, 3, 4, 5, 6].

For such a selective excitation, a high-intensity and narrow-band light source with wavelength tunability is necessary. However, in the mid-infrared range, which is difficult to cover with a conventional laser system, a suitable light source has not been established at present. A widely used light source in the mid-infrared range has been the CO<sub>2</sub> laser [7]. Although it can produce several 10 kilowatts of power, the wavelength is fixed at 10.6  $\mu\text{m}$ . A new technology that has been developing recently is the quantum cascade laser (QCL). It can serve as a compact light source and is expected to be used widely. It can produce 1 W of power in continuous operation in the ap-

proximately 8  $\mu\text{m}$  wavelength range [8]. The wavelength can be changed by modifying the design of the quantum structure of the chip; however, it does not offer wavelength tunability in operation.

One of the promising approaches is the free-electron laser (FEL) [9, 10]. Although it requires an accelerator system and requires a larger facility compared with a conventional laser-based system, it can produce a high radiation power originating from the beam power, and the wavelength can be tuned by the undulator setting or the beam energy. Several infrared FEL facilities have been operating [11, 12, 13, 14, 15, 16]. FEL systems used in these facilities are the optical-cavity-type FEL, which uses a multi-bunch electron beam, and the radiation is amplified in an optical cavity through interactions with many bunches. The advantage of the cavity-type FEL is that it can reach a high power even with a low single pass gain, and hence the requirement for electron beam quality can be relaxed. On the other hand, precise optical cavity tuning is necessary to match the radiation and electron beam in three dimensions. Changing the wavelength sometimes requires machine tuning, and real-time tunability can be a problem. The cavity-type FEL emits multi-pulse output. When one wishes to measure the fast response of material in a single radiation pulse, a special technique, such as a fast switch mirror, must be developed [17].

The technologies of the superconducting RF accelerator have been widely developed. When combined with a high-

quality electron source, which has also been developed recently [18], it is possible to realize a high-quality electron beam at a high repetition rate. Such an electron beam is suitable for use with an FEL working in a single-pass layout of the self-amplified spontaneous emission (SASE) scheme at a high repetition rate.

The mechanism of SASE was first explored in the infrared range [19, 20, 21, 22, 23]. The SASE FEL has now been widely operating in the X-ray range. However, it has not usually been applied in the long-wavelength range. One of the difficulties of the SASE FEL in the long-wavelength range is the time slippage effect in the long undulator. The electron beam is delayed relative to the radiation pulse by one wavelength for each period of the undulator. This effect becomes important when the radiation wavelength is long. The overlap between the electron bunch and the radiation pulse, which is essential for the FEL gain, is limited by the slippage effect.

Recently, a sub-femto second X-ray FEL has been required for the investigation of fast electron dynamics within atoms and molecules. In such a regime, the slippage effect becomes important even at short wavelengths. In such a short-pulse X-ray FEL, it has been recognized that the undulator tapering scheme is effective in optimizing the efficiency of interaction between the radiation and the electron beam in the time slippage [24, 25, 26, 27]. When the relationship between the bunch length, the radiation wavelength, and FEL gain length is scaled, there are similarities between the sub-femto second X-ray FEL and a mid-infrared SASE FEL. The techniques established for a short-pulse X-ray FEL may be useful for the mid-infrared case, and vice versa.

The cERL [28] at KEK is a test accelerator of an energy-recovery linac (ERL [29]) configuration with a cw superconducting linac. It can serve as a model for a future high-beam power accelerator utilizing the ERL scheme. To demonstrate mid-infrared SASE FEL operation in the modern design of the accelerator, we constructed an experimental setup of the SASE FEL in the return loop of the cERL. The typical layout of the ERL includes a function for controlling the bunch length with an off-crest operation of the linac cavity and dispersion tuning in the arc section [30, 31, 32, 33]. We established FEL beam tuning by utilizing this function. The layout at the cERL is not ideal for the FEL. Due to the relatively low beam energy and the long beam path, the bunch suffers strong space charge effects through the transport line. To manage this adverse circumstance and increase the FEL output power, we introduced the undulator tapering technique assuming that the energy chirp in the bunch will be counteracted by the tapering. Finally, we performed a demonstration experiment using FEL irradiation with a test sample. It confirmed the establishment of FEL beam tuning and operational stability.

The most important advantage of the ERL is the possibility of handling a high average beam power. Because the beam-to-radiation power conversion efficiency of the

FEL is quite low, especially in the short-wavelength range, a very large beam power will be necessary for a high-average-power FEL, which is required for extreme ultraviolet (EUV) lithography [34]. An SASE FEL in an ERL scheme is a candidate for serving as such a light source within a reasonable total electric power and beam dump system. Demonstration of the SASE FEL, even at a long wavelength, would be a first step in the development of an EUV lithography facility.

In this paper, we first describe the initial design of the FEL followed by its detailed simulation in Sec. 2. Then in Sec. 3, we describe the experimental setup of the FEL system at the cERL. Sec. 4 is about beam tuning and the performance of the FEL. The results are discussed and summarized in Sec. 5. The Sec. 6 concludes the paper.

## 2. DESIGN OF THE SYSTEM

### 2.1. Conceptual Design of SASE FEL

We began the design of this experiment assuming the boundary conditions of the existing cERL facility. The target wavelength of the FEL was set to the mid-infrared range. The targeting central wavelength was set to 20  $\mu\text{m}$ , considering the electron beam energy of 17.5 MeV.

Before performing a detailed simulation, we conducted a simple estimation based on a one-dimensional steady-state formula assuming the following expected beam and undulator parameters: The bunch charge is  $Q = 60$  pC. The transverse RMS beam size is  $\sigma = 0.2$  mm. The RMS bunch length is  $\sigma_t = 1.0$  ps. The undulator strength is  $a_w (= K/\sqrt{2}) = 1.0$ . The undulator period is  $\lambda_u = 24$  mm. The Pierce parameter  $\rho$  then becomes [35]

$$\rho = \left( \frac{\bar{\kappa}^2 a_w^2 \lambda_u^2 j_0}{16\pi\gamma^3 I_0} \right)^{1/3} \sim 0.01, \quad (1)$$

where  $\bar{\kappa} (= [JJ]) \sim 0.86$ ,  $I_0 = mc^3/e \sim 17$  kA, and  $j_0 = Q/(2\pi\sigma^2\sqrt{\pi}\sigma_t)$ . The FEL gain length becomes  $L_g = \lambda_u/(4\pi\sqrt{3}\rho) = 0.1$  m. The saturation length is  $L_{sat} = \lambda_u/\rho = 2.1$  m.

However, the slippage in one saturation length becomes 5.8 ps, which is much larger than the bunch length. In view of this, the above steady-state estimation needs a major correction. We moved to a time-dependent simulation that includes the slippage effect with a finite bunch length assuming a Gaussian-shaped bunch. Figure 1 plots the FEL power development along the undulator. It shows that more than 5 m of undulator length is necessary to reach the saturation point. Considering practical issues, such as cost and lead time, in fabricating one long undulator, we decided to use two 3-m undulators.

### 2.2. Simulation of SASE FEL

A detailed description of the layout will be given in Sec. 3 and [28]. For the start-to-end simulation, i.e., from the cathode of the gun to the end of FEL undulator including

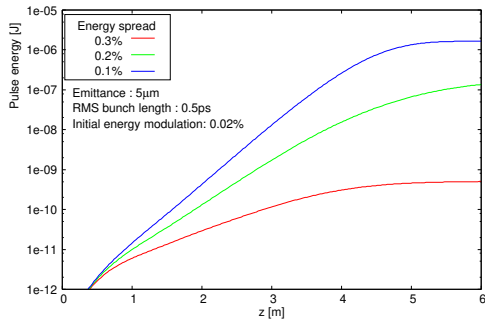


Figure 1: Simulation for estimating required length of undulator. Development of FEL power along the undulator was calculated in a layout including a 6 m undulator and a matched beam for it, assuming realistic beam quality.

the development of FEL radiation, we used three simulation codes. The injector part where the beam energy is low was implemented using GPT [36]. After the main linac, the particle distribution was passed to elegant [37], which was suitable for tracking the beam transport system up to the entrance of the FEL undulator. The distribution was then used as the input of FEL simulation by GENESIS [38]. The final calculation was performed with 500k macro particles.

The particle distribution of the optimized injector setting was simulated using GPT. The simulated particle distribution at the entrance of the second main linac cavity was used as the starting point in the elegant simulation. Figure 2 shows the longitudinal phase space distribution. It is clear that the beam has an energy chirp in the bunch.

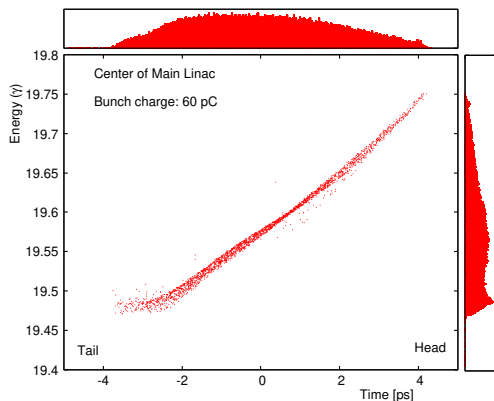


Figure 2: Simulated particle distribution at the center of the main linac using GPT. The particle distribution in the longitudinal phase space of time and energy is shown. The shapes projected on each axis are also shown.

From the entrance of the second main linac, the tracking simulation was performed using elegant. It includes the longitudinal space charge effect (LSC) and the coher-

ent synchrotron radiation effect (CSR), but the transverse space charge effect (TSC) was ignored. The TSC is not negligible; in this case, however, it can be locally corrected as a perturbation from the viewpoint of Twiss parameter tuning as explained in Appendix A. In this tracking, the procedure of beam handling for bunch compression, i.e., the RF phase of the main linac and the longitudinal dispersion ( $R_{56}$ ) tuning in the arc section, was included.  $R_{56}$  is defined by  $R_{56} = dl/d\delta$ , i.e., the path length ( $l$ ) difference depending on the relative energy ( $\delta$ ) variation.

The FEL simulation was performed using the time-dependent calculation of GENESIS. The layout consists of two undulators and the space between them. The simulations were conducted in three steps. The first step was for the first undulator using the particle distribution received from elegant as the initial distribution. To reproduce the start-up effect due to the fine density distribution that may not appear in the particle distribution, we employed an empirical parameter to set the initial energy modulation. In the second step, using the particle distribution at the exit of the first undulator, the tracking calculation in the space between the undulators was performed. At this time, the radiation data were removed because they do not overlap with the electron bunch in time after the space. In the third step, the simulation of the second undulator was conducted using the particle distribution above as the input. The radiation began growing from zero.

Although we performed many simulations in the designing stage, the actual parameters realized in the beam experiments have changed after the beam tuning explained in Sec. 4. Here, we show the simulation results for the beam parameters corresponding to the experimental case. The parameters used in the simulation are summarized in Table 1.

Figure 3 shows the simulation results of FEL output power along the longitudinal position. The start-up can be changed by the energy modulation we set empirically. The gain at the second undulator is estimated as approximately 10 for any case.

The particle distribution in the longitudinal phase space at the exit of the second undulator is shown in Fig. 4. Due to the microbunching instability, the phase space distribution has a complicated structure with kinks. When strong FEL interaction has occurred, the energy of the electron beam should be modulated at the radiation wavelength. Such a fine structure of energy modulation appears at several locations in the bunch. It appears that some localized parts of the bunch independently contribute to the FEL gain. If the whole bunch could contribute to the growth of a single spike of radiation pulse, the efficiency would become much higher. However, in the given scenario of a complicated distribution with a large energy spread, the signal can grow only locally. This simulation case shows that even if the situation is not ideal, there is still a chance to obtain an FEL gain.

The radiation spectrum can be obtained by Fourier analysis of the radiation field data extracted from the simula-

Table 1: Parameters used in the simulation

Initial distribution		
Bunch charge		60 pC
Norm. Emittance (X)		1.63 $\mu\text{m}$
Norm. Emittance (Y)		2.01 $\mu\text{m}$
Bunch length		1.85 ps (RMS)
Energy spread	$\Delta\gamma/\gamma$	$2.23 \times 10^{-3}$ (RMS)
Transport		
Chirp phase		+29° (at 1.3 GHz)
$R_{56}$		-0.282 m
Entrance of Undulator		
Energy	$\gamma$	34.46
Norm. Emittance (X)		4.45 $\mu\text{m}$
Norm. Emittance (Y)		1.85 $\mu\text{m}$
Bunch length		1.94 ps (RMS)
Energy spread	$\Delta\gamma/\gamma$	$6.22 \times 10^{-3}$
Energy modulation		0.02%
Undulator		
Strength	$a_w$	0.97
Tapering coefficient		-0.048
Period	$\lambda_u$	24 mm
Length		3 m $\times$ 2

tion. Figure 5 shows the results. The bandwidth was estimated as 0.8  $\mu\text{m}$  in full width at half maximum (FWHM). The center wavelength can be changed by the undulator strength. The spectrums show multiple peaks, which may be attributed to the local power growth explained in Fig. 4. Figure 6 shows the simulated radiation pulse shape. It turns out not to be a simple single spike. It appears that the signal is composed of several pulses that have independently grown at different parts in a bunch.

Figure 7 shows the spatial power distribution at 1.08 m downstream from the exit of the second undulator, which corresponds to the position of the extraction mirror. The diameter of the profile is approximately 20 mm.

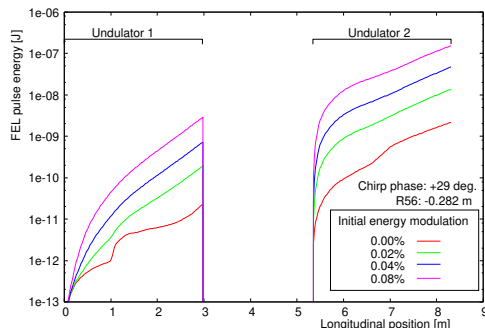


Figure 3: Simulated FEL power development along the undulator based on the beam parameters determined in the experiment, chirp phase of +29° and  $R_{56}$  of -0.282 m. The initial energy modulation is an empirical parameter to adjust the absolute power using the start-up effect. The radiation wavelength was set to 20  $\mu\text{m}$ .

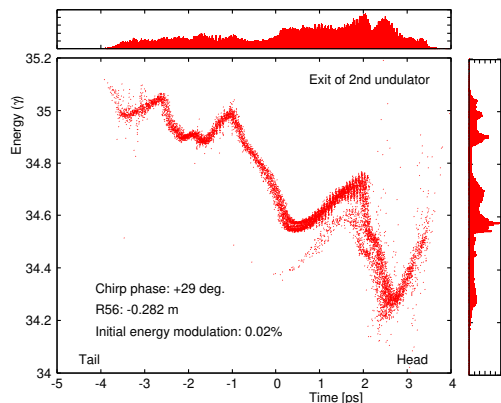


Figure 4: Longitudinal phase space distribution at the exit of the undulator. The shapes projected on each axis are also shown. Fine structures corresponding to the radiation wavelength are formed by FEL interaction, showing that some localized parts contribute to the FEL gain. The radiation wavelength was set to be 20  $\mu\text{m}$  in this calculation.

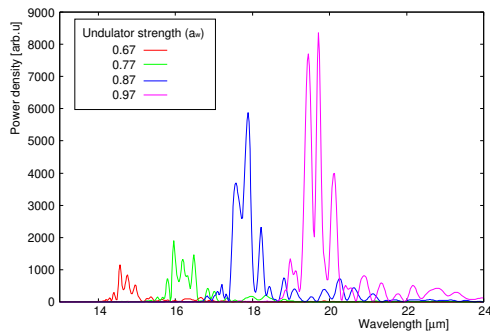


Figure 5: Simulation results of the radiation spectrum. Four cases of undulator strength are shown.

### 3. EXPERIMENTAL SETUP

#### 3.1. Beam transport system

Since the initial construction [28], the cERL has been operating as a test accelerator with its layout being changed in every few years [39, 40]. Figure 8 shows the layout for the FEL experiment. The downstream half of the straight line in the return loop was modified.

The designed beam optics of the return loop is shown in Fig. 9. This beam optics was calculated starting from the Twiss parameters at the exit of the main linac, and transported by linear optics without any collective effects. The arc section consists of four 45° bending magnets, six quadrupoles, and two sextupoles. The linear optics was designed to be mirror symmetric about the center of the arc. It was designed to be achromat and to be  $R_{56}$  controllable by changing the strength of the quadrupole magnets in the arc section.

For the FEL beam tuning, where the longitudinal density distribution in the bunch is important, the  $R_{56}$  tuning

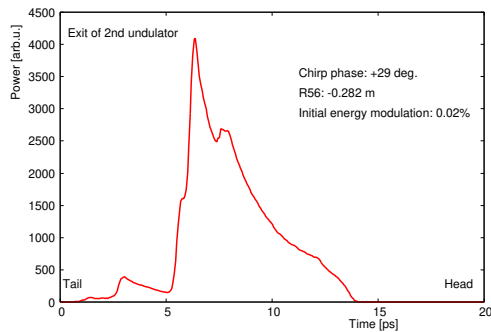


Figure 6: Simulated radiation pulse shape at the exit of the second undulator. The pulse shape contains several (more than three) peaks. Each of the peaks appears to originate from a different part of the bunch. The radiation wavelength was set to  $20 \mu\text{m}$  in this calculation.

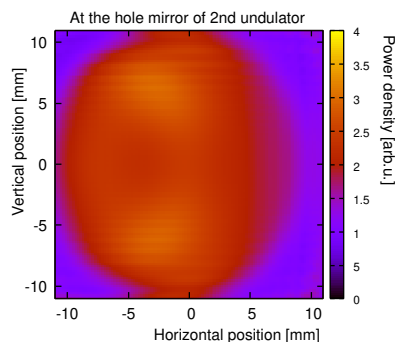


Figure 7: Spatial profile of radiation power density at the extraction hole mirror of the second undulator. The radiation wavelength was set to be  $20 \mu\text{m}$  in this calculation.

is a sensitive knob that optimizes the FEL output. The details of the design and tuning of bunch compression will be given in elsewhere [41]. For fine beam optics tuning to the undulators, four quadrupole magnets upstream of each undulator were chosen to control four degrees of freedom. They were used as combined knobs, as explained in Appendix C.

### 3.2. Layout of FEL section

The layout of the FEL section is shown in Fig. 10. Two 3-m undulators were located with a separation of 2.3 m. Various components were installed in the short space between the undulators, The installed components were a hole mirror system to extract radiation and that can also be used as a beam profile monitor, four quadrupole magnets for optics matching to the second undulator, and a chicane magnet that could help enhance the FEL power with the optical klystron effect [42].

We adopt a planar-type undulator in the horizontal plane, utilizing the adjustable phase scheme (APU [43]). The effective strength of the vertical magnetic field can be varied by sliding the relative position (we call it as phase

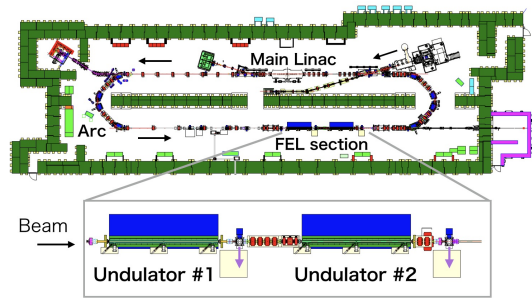


Figure 8: Layout of cERL. The electron beam from the injector is first accelerated by the main linac. Next, it is transported to the return loop through the arc section to the newly constructed FEL section.

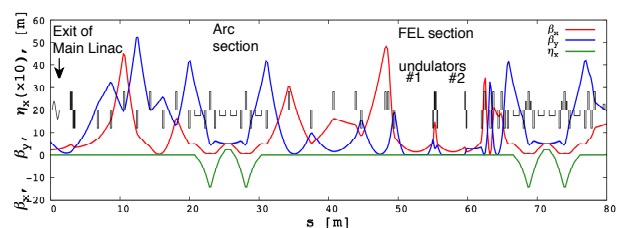


Figure 9: Designed beam optics of the return loop, starting from the exit of the main linac to the exit of the second arc. The beta functions of the horizontal and vertical plane and the dispersion function of horizontal plane are shown.

by defining the position shift of one period to be  $2\pi$ ) of the girder of each side while the mechanical gap is fixed as

$$a_w = a_{w0} \cos(\text{phase}/2) \quad . \quad (2)$$

In the case of low beam energy, the vertical focusing effect of the undulator becomes strong. It is necessary to carefully match the Twiss parameter to maintain the small beam size throughout the undulator, and also to connect the beam condition downstream. The vertical motion of the beam is represented as an oscillation equation:

$$\frac{d^2 y}{ds^2} = - \left( \frac{2\pi a_{w0}}{\lambda_u \gamma} \right)^2 y \quad , \quad (3)$$

where the  $a_{w0}$  is the undulator strength at the maximum effective field. The focusing effect does not change even

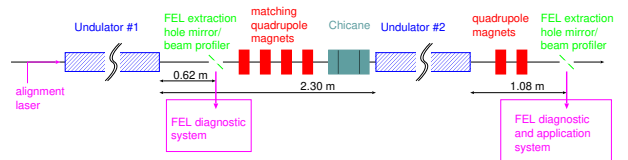


Figure 10: Layout of the FEL section. A FEL extraction mirror, matching quadrupoles, and a chicane magnet are installed in the 2.30 m space between the two 3-m undulators. The second FEL extraction mirror is installed behind of two quadrupole magnets.

if the effective field is reduced by sliding the poles of the APU. This feature is an advantage of the APU, especially for the ERL layout, where the beam condition in downstream must be controlled well while changing the FEL wavelength.

The undulators were newly fabricated for this experiment. Figure 11 shows the experimental setup. To obtain the magnetic field strength for the undulator period that corresponds to the target radiation wavelength at the given beam energy, a relatively small gap of 10.0 mm was required. The undulator was modified so that the magnetic field strength was tapered along the beam axis. The tapering was achieved by inclining the whole upside girder on the support structure to obtain a linear variation in the gap. The tapering coefficient was designed to be  $-0.048$ , which means that the field strength at the exit was higher by the ratio with respect to that at the entrance. Both the undulators were modified to have the same tapering coefficient. The parameters of the undulator are summarized in Table 2.

Table 2: Parameters of the undulator

Type		Planar (APU)
Gap		10.0 mm (fixed)
Strength (maximum)	$a_w$	$0.97 (= K/\sqrt{2})$
Tapering coefficient		-0.048
Material		Nd-Fe-B
Number of period		124
Period	$\lambda_u$	24 mm
Number of unit		2

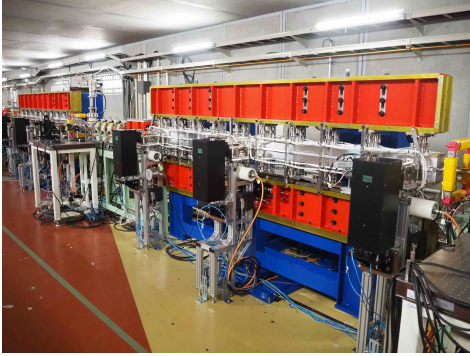


Figure 11: Undulators viewed from downstream of the second undulator. The three boxes placed at the side of each undulator are for the beam profile monitor systems.

The small gap of the undulators required the vacuum duct in the undulators to have a flat cross section with thin walls, as shown in Fig. 12. The duct is made of aluminum alloy fabricated by the extruded technique. The inner cross section of the duct has an elliptical shape with diameters of 50 mm and 7.8 mm in the horizontal and vertical directions, respectively. Figure 13 shows the structure of the undulator duct. Beam profile monitors, each of

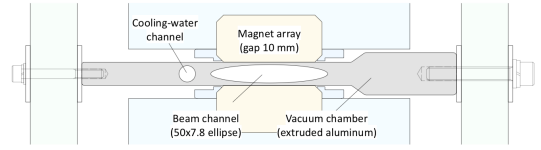


Figure 12: Cross section of the undulator and the vacuum duct.

which consists of a scintillator insertion system and a window to monitor it using a camera system, were installed at three locations in each of the undulator ducts. The profile monitors were located at the center of the undulator and 0.15 m from both ends of the undulator pole edge. The scintillators are Ce-doped YAG crystal of 0.1 mm thickness. The effective area of the scintillators is  $30 \text{ mm} \times 4 \text{ mm}$  and they have a racetrack shape. They are inserted in  $45^\circ$  with respect to the beam direction, and are viewed from the rear.

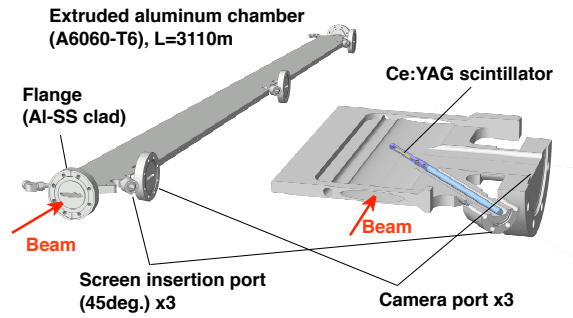


Figure 13: Structure of the vacuum duct in the undulator. It includes ports for three beam profile monitors. Each beam profile monitor part consists of a  $45^\circ$  screen insertion port and a camera viewing port. (Based on production drawings of SAES Getters S.p.A. and SEAS RIAL Vacuum S.r.l. )

An FEL radiation output system was installed after each undulator. Radiation was extracted to the air through the KRS-5 window by reflecting it in the perpendicular direction with a hole mirror as shown in Fig. 14. A gold-coated SUS plate of dimensions  $46 \text{ mm} \times 50 \text{ mm}$  with a circular hole of 8 mm diameter viewed from the beam was inserted on the beam axis. According to the simulation of Fig. 7, 95% of the radiation power can be extracted without destroying the electron beam. The hole mirror can be switched to a beam profile monitor which is a Ce:YAG scintillator viewed from the rear through an SUS mirror so that the electron beam size can be measured. A camera system monitors the setup from the window at the opposite side of the radiation extraction.

To match the beam optics to the second undulator, four quadrupole magnets of 100 mm thickness were located be-

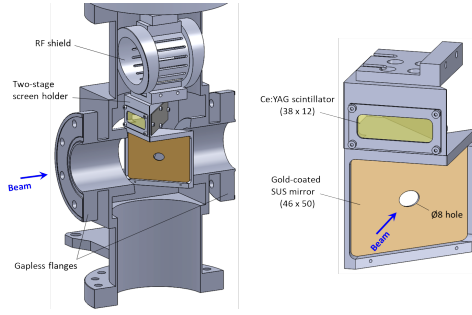


Figure 14: Structure of the insertion system for the FEL extraction hole mirror system. The gold-coated mirror with a hole of 8 mm diameter is inserted on the beam axis at  $45^\circ$  to reflect the FEL radiation in the perpendicular direction. The system can be inserted in two positions. The other position is for the Ce:YAG scintillator to measure the electron beam.

tween the undulators. They were set in a Defocus-Focus-Defocus configuration for the horizontal plane, it actually composed a triplet optics.

A chicane bump system consisting of three dipole magnets (as explained in Fig. 15) was also installed between the undulators. The role of the chicane in a typical FEL is as a phase shifter to match the phase of the radiation between the undulators. However, its role is different in our case, where radiation from the first undulator totally slips the bunch duration, and there is no overlap at the second undulator. The chicane was installed in anticipation of the effect of the optical klystron; i.e., the density modulation initiated by the energy modulation after the first undulator could be enhanced, which could help increase the FEL output. The maximum bump height within the fiducial volume is 23 mm, which corresponds to an  $R_{56}$  of 6 mm.

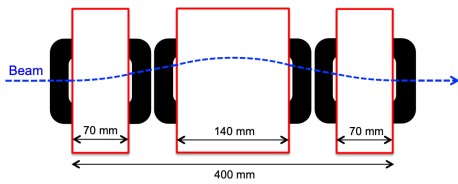


Figure 15: Chicane magnet. Three dipole magnets produce a closed bump in the horizontal plane.

### 3.3. FEL diagnostic system

The radiation output port downstream of the first undulator was prepared primarily for beam tuning. Figure 16(a) shows the layout of the setup. The radiation reflected from the beam axis by the hole mirror was extracted to the air through a KRS-5 window of 5 mm thickness. First, it was focused by a parabolic mirror. Three filters, a band-pass filter (BPF) and two ZnSe plates, were

located at the focal point. The BPF removed the radiation contributed by mechanism other than the FEL. The center wavelength and bandwidth of the BPF were designed to be  $20 \mu\text{m}$  and 10%. The ZnSe plates were used as attenuators for the  $20 \mu\text{m}$  radiation to avoid detector saturation. The radiation was then again focused by a parabolic mirror, and it was detected by a HgCdTe detector and a pyroelectric sensor. The two detectors were mounted on a common three-axis stage.

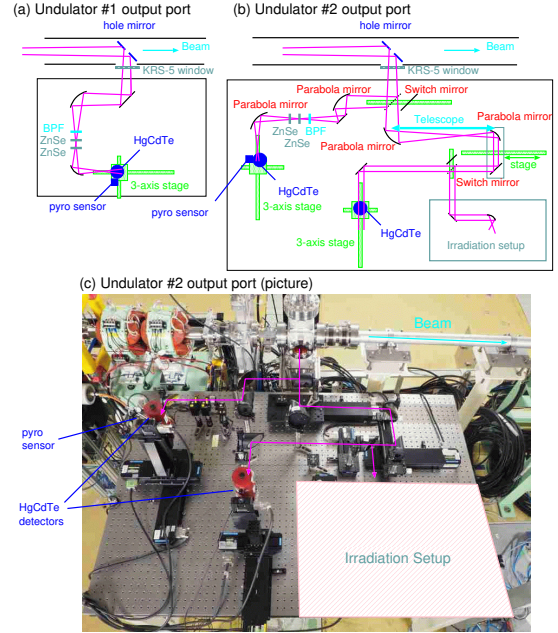


Figure 16: Setup of the radiation diagnostic system. The basic design of the monitor system is the same. It consists of focusing optics with a parabolic mirror, three filters placed at the focal point, and another parabolic mirror to focus on the detectors on a three-axis stage. The system at the second undulator has the irradiation system behind the switch mirror.

The radiation output port downstream of the second undulator was prepared for the final FEL output. A radiation measurement system and an application system were prepared on the table. Figure 16(b) shows the layout of the setup. The basic design was the same as the upstream design. The first mirror switched the path to either of the two setups. The reflection path was for a measurement system similar to that of the first undulator. The transmission path (in the case without the switching mirror) was prepared for sending the radiation to the irradiation system. Figure 16(c) shows the table for the second undulator.

To align the optical setup at the two systems, a guide laser was prepared. A He-Ne laser was placed upstream of the first undulator. The guide laser was placed on the beam axis through the undulators, as shown in Fig. 10. If the hole mirrors at the FEL output ports were inserted with some offset for shifting the hole from the axis, the guide laser was extracted to the radiation measurement

systems. The initial optical alignment of the measurement systems was performed with this guide laser.

The HgCdTe detector (FTIR-24-1.0) is a product of In-fraRed Associates. It was used at the temperature of liquid nitrogen and was assembled with a dewar for 12 h operation. A dedicated preamplifier was placed near the detector. The voltage pulse signal was then recorded with an oscilloscope. The sensitive wavelength range was between 7 and 24  $\mu\text{m}$  with the KRS-5 window model. The maximum sensitivity was at a wavelength of 15  $\mu\text{m}$ . The sensor size of the HgCdTe detector is 1 mm  $\times$  1 mm. By scanning the detector in the horizontal and vertical directions, the spatial profile of the radiation can be obtained. By repeating the measurement while changing the longitudinal position of the detector, we can set the detectors at the focal position.

The pyroelectric detector (QE8SP-B-MT-D0, M-Link) is a product of Gentec Inc. The sensor was connected to its amplifier, and the amplified analog output was recorded with an oscilloscope. Because the time constant of the detector was much longer than the beam macro-pulse duration, the measured signal corresponds to the total energy of the macro-pulse. The sensor size of the pyroelectric detector is 7.8 mm  $\times$  7.8 mm. After confirming that the spot size was sufficiently small compared with the sensor size, we switched the detector from the HgCdTe to the pyroelectric sensor for the absolute energy measurement. Calibration of the pyroelectric detector was performed before the beam experiment. Using an infrared (976 nm wavelength) laser of known pulse energy and similar pulse shape as the beam, the output voltage of the amplifier could be calibrated taking into account the spectrum difference in the absorption constant of the sensor material.

### 3.4. Application demonstration setup

To optimize the spot size and divergence of the FEL radiation for the irradiation setup, a telescope system was prepared. The FEL output from the second undulator was first focused with a parabolic mirror of 230 mm focal length, and then converted to a collimated light with a parabolic mirror of 100 mm focal length at the over-focus position. The distance between the parabolic mirror pair can be controlled remotely to adjust the divergence downstream. A switch mirror downstream of the telescope system reflects the radiation to the irradiation system, while the radiation is sent to the measurement system of the HgCdTe detector on a three-axis stage if the switch mirror is off the line. The spatial profile and the divergence can be measured by scanning the detector.

To investigate the effect of irradiation of mid-infrared FEL pulse, and the nonlinear response of materials to high-peak-intensity mid-infrared radiation, the FEL irradiation system was developed. Figure 17 shows the setup. It consists of a parabolic mirror of 25.4 mm diameter and 50.8 mm focal length, to tightly focus the radiation on the sample and a remote control stage system for setting the samples. Samples for the irradiation experiment, typically

plates of 50 mm  $\times$  50 mm, can be set on the stage. A microscope system was prepared to monitor the sample in real time during the experiment. A remote control shutter was prepared at the entrance of the system to precisely control the irradiation time for the sample.

To confirm the spot size on the sample, a knife-edge scan system [44] was developed. Two mutually perpendicular knife edge plates were mounted on the sample stage instead of the sample. A pyroelectric detector was set behind the sample stage.

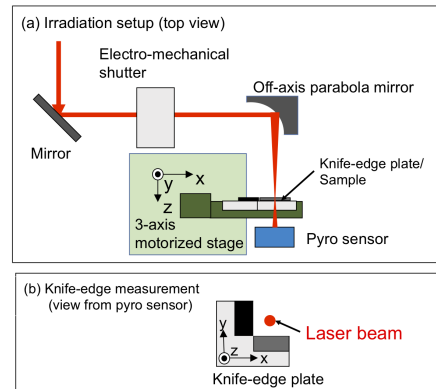


Figure 17: Setup for the irradiation experiment. The FEL radiation is tightly focused on the sample by the parabola mirror. The sample can be moved with the three-axis stage. In the knife-edge beam size measurement, the sample was replaced with a plate with mutually perpendicular knife edges.

## 4. EXPERIMENT

### 4.1. Beam Tuning

#### 4.1.1. Beam transport tuning and measured beam performance

In this series of experiments, the beam was operated in burst mode, where all the components of the accelerator system were operated in continuous mode except for the laser system of the electron gun [28]. This mode of operation was to enable beam operation allowing for beam loss. The electron beam was emitted as a macro-pulse of 130 bunches with a 1.3 GHz fundamental repetition frequency. The macro-pulse was emitted at 5 Hz. The bunch charge and macro-pulse duration were confirmed at the Faraday cup located just downstream of the gun.

The upstream beam, starting from the gun cathode to the exit of the main linac, was separately optimized by simulations. Based on the simulation for the space-charge-dominated beam, procedures to tune the beam from upstream were developed. Here, we begin our description from the tuning of the second main linac cavity.

To set the longitudinal energy chirp in the bunch, we first surveyed the RF phase of the second main accelerator cavity. Figure 18 shows the dependence of the horizontal beam size at a dispersive position in the arc section



on the RF phase while the beam energy is retained by simultaneous adjustment of the RF amplitude. The minimum condition of the horizontal beam size corresponds to the phase where the energy chirp is almost zero (according to the simulation, it corresponds to  $+2^\circ$  off from the minimum condition of the energy spread). This condition defines the origin of the phase, called as the chirp phase, in our discussion. We set the RF phase to the positive direction, which corresponds to the case that the bunch head has higher energy than the tail. The chirp phase is an important parameter to control bunch compression. After rough trials to survey the starting condition before fine beam tuning for maximizing FEL, we set our starting point of the chirp phase.

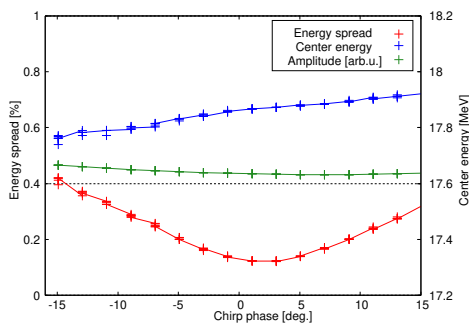


Figure 18: Measurement of the energy spread as a function of RF phase of the second main linac cavity. The horizontal beam size and position at the profile monitor in the beginning of the arc section were measured.

In the following, we show the measured beam parameters obtained after FEL maximization tuning, which will be explained in Sec. 4.1.2. The results are summarized in Table 3.

Table 3: Measured beam parameters after FEL optimization

Bunch charge	60 pC/bunch	
Exit of Main linac		
Norm. Emittance (X)	$\epsilon_x$	$3.27 \pm 0.17 \mu\text{m}$
Norm. Emittance (Y)	$\epsilon_y$	$1.57 \pm 0.05 \mu\text{m}$
Energy spread	$\Delta\gamma/\gamma$	0.6%
Total Energy	$\sigma_t$	17.7 MeV
Transport		
Chirp phase	$+29^\circ$	
$R_{56}$	$-0.282 \pm 0.046 \text{ m}$	
Entrance of Undulator		
Norm. Emittance (X)	$\epsilon_x$	$5.55 \pm 0.19 \mu\text{m}$
Norm. Emittance (Y)	$\epsilon_y$	$5.11 \pm 0.16 \mu\text{m}$
Bunch length (RMS)	$\sigma_t$	$\sim \text{ps}$ (0.6 ps structure)

The energy spread was measured by the horizontal beam profile at a dispersive position in the arc section. At the

profile monitor, the horizontal dispersion and beta function were calculated as  $\eta_x = 0.49 \text{ m}$  and  $\beta_x = 1.9 \text{ m}$ , respectively. The horizontal beam size was dominated by the dispersion term. The RMS energy spread was estimated as 0.63%. Note that the energy spread included contribution of the whole macro-pulse. The beam loading effect of macro-pulse charge,  $60 \text{ pC} \times 130$  bunches, can change the accelerating field in RF cavities along the bunch train. By calculating the beam loading effect, the beam energy change from pulse head to tail is estimated as 0.5%. In the energy spread measurement, a contribution of 0.14% in RMS was made by this pulse-to-pulse effect.

Because the arc section is designed to have a strong vertical focusing, the beam profile and divergence after the arc are sensitive to the transverse beam parameters at the arc entrance. The orthogonal combined knobs using four quadrupole magnets just before the arc were prepared as explained in Appendix C. Figure 19 shows the beam profile measured at the arc entrance, at the center, and at the exit. It shows that the symmetric optics with respect to the arc center was successfully been realized.

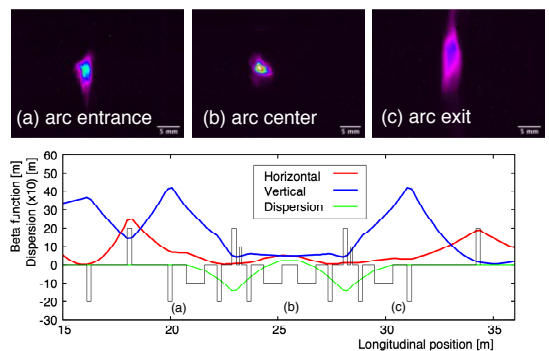


Figure 19: Beam profiles in the arc section. The arc was designed to be symmetric with respect to the center.

To confirm the achromat condition of the arc, the transverse dispersion was measured. The RF amplitude of the second main linac cavity was changed to shift the beam energy by  $-1\%$ , and the beam position change was measured by the beam position monitors. In this measurement, sextupole magnets were set off because they introduce a strong nonlinear effect in this measurement of a relatively large orbit change. Figure 20 shows the results of the measurements, which confirmed that the dispersion at downstream of the arc and coupling in the vertical direction were small. We also confirmed that the achromat condition was retained while the  $R_{56}$  knobs were being changed. From the symmetric design of the arc, the transverse dispersion at the center of the arc  $\eta_c$  and the  $R_{56}$  of the arc are related by  $R_{56} = 1.414\eta_c - 0.34 \text{ [m]}$ , in the present case [45]. By measuring  $\eta_c$ , the  $R_{56}$  of the arc can be estimated indirectly. The  $R_{56}$  at the FEL power maximum was estimated as  $-0.282 \pm 0.046 \text{ m}$ .

The beam emittance just upstream of the FEL section was measured by the waist scan method using a

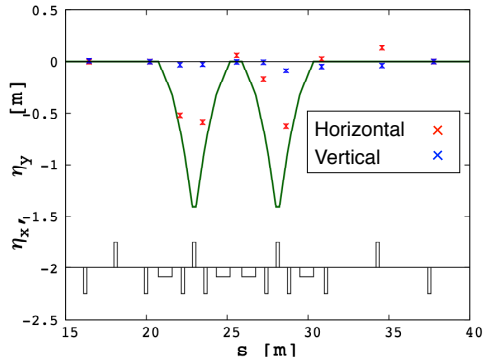


Figure 20: Dispersion measurement at the arc section. The beam energy dependence of the transverse beam orbit was measured by the beam position monitors.

quadrupole magnet and a profile monitor [39]. Figure 21 shows the results. By fitting the data with a hyperbolic function, the normalized emittance was estimated as  $\epsilon_x = 5.55 \pm 0.19 \mu\text{m}$  and  $\epsilon_y = 5.11 \pm 0.16 \mu\text{m}$  for the horizontal and vertical directions, respectively. The emittance measured at just downstream of the main linac using a similar method resulted in  $\epsilon_x = 3.27 \pm 0.17 \mu\text{m}$  and  $\epsilon_y = 1.57 \pm 0.05 \mu\text{m}$  for the horizontal and vertical directions, respectively. There was some emittance degradation in the beam transport, but, the effect was still within the manageable range.

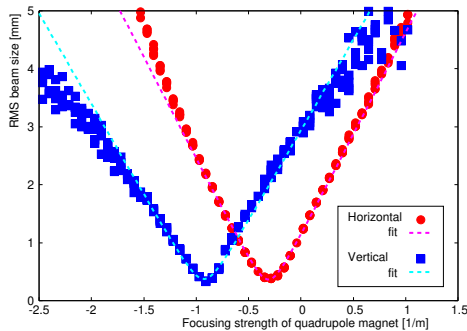


Figure 21: Measurement of emittance at the upstream of the FEL section. The beam size at the screen monitor was measured while the strength of a quadrupole magnet was being scanned. The line is the fitting result obtained by using a function  $\sqrt{a(K-b)^2 + c}$ , leaving  $a$ ,  $b$ , and  $c$  as free parameters.

The bunch length is an important parameter for the FEL. However, the existing setup did not have an instrument to measure the bunch length directly. We used coherent radiation as an indirect tool to evaluate the bunch length. A terahertz interferometer system using coherent transition radiation (CTR) was developed approximately 10 m upstream of the FEL undulator in the same straight section [45]. By detecting the autocorrelation with a Michelson interferometer, the spectrum of the bunch can

be obtained. Figure 22 shows the interferogram data and the results of the fitting analysis. It shows an RMS bunch length of  $\sigma_t = 0.585 \pm 0.016$  ps. To check the bunch length measurement in a relatively direct way, we tried measuring incoherent transition radiation in the visible range using a streak camera system. Although the measurement was performed in a different beam operation period, and hence the details of beam tuning were not exactly the same, the typical beam parameters were similar. The result was never shorter than 1.6 ps in RMS. Comparing the results obtained with the streak camera with those obtained with the interferometer, we infer that the scale of the whole bunch size was in the range of a few picoseconds, and it had small longitudinal structures of 0.6 ps scale at the same time.

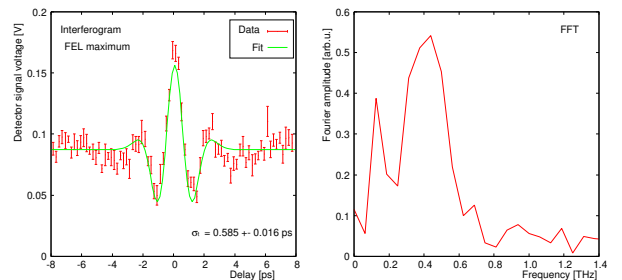


Figure 22: Autocorrelation signal of CTR interferometer (left) and its spectrum (right). By fitting the data with a model function of low-frequency cutoff, the RMS bunch length of the core part of the bunch can be estimated indirectly.

The transverse beam matching to the undulator was performed using four orthogonal knobs while measuring the screen monitor in the undulator duct. Figure 23 shows a typical result after the tuning. It shows that the vertical beam size remained constant as the vertical Twiss parameters matched to the undulator focusing, and that the horizontal beam size become minimum at the center of each undulator to minimize the averaged beam size in the undulator.

#### 4.1.2. FEL power maximization tuning

We explain the beam tuning procedure for FEL power maximization in the following. Once the beam condition has been established to pass the undulators with a reasonable beam size and position, the tuning procedure was switched to the scheme based on the FEL radiation measurements.

To perform the beam tuning efficiently, we have prepared several knobs for use in the beam operation among the many control parameters in the complicated accelerator system. The knobs routinely used were as follows:

- The  $R_{56}$  knob changes the quadrupole magnets in the arc. Because  $R_{56}$  changes the longitudinal distribution of the bunch, it is a sensitive knob for the FEL.

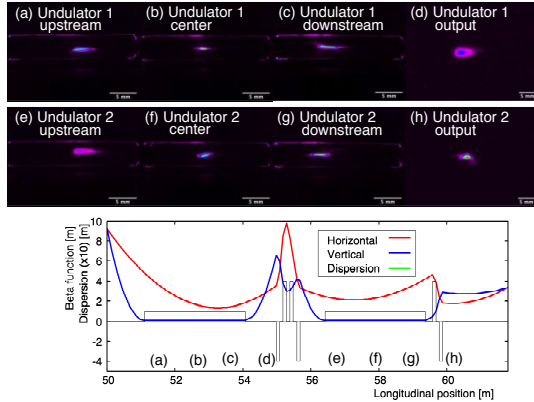


Figure 23: Beam profile at the FEL section. Three screen monitors in each undulator duct were used to confirm beam optics matching. The two FEL output ports at downstream of each undulators also have screen monitors.

- The SX knobs were the two sextupole magnets in the arc section. They change the higher-order terms of the transverse dispersion, as a result of which the shape of the longitudinal phase space distribution changes nonlinearly.
- Matching knobs for the first and second undulator are the orthogonal combined knobs with four quadrupole magnets. They change the average beam size along the undulator, and should affect the FEL gain.
- The injector RF parameters, namely, the phase and amplitude of the buncher and the first cavity in the injector module. Because the velocity bunching at the low-energy section is sensitive to the initial bunch length, they are sensitive parameters for the FEL.
- The RF phase and amplitude of the second cavity in the main linac. They shift the chirp phase from the one initially chosen only after a rough survey.
- Steering dipole magnets at the entrance of each undulator. They change the position and angle of the incoming beam orbit in both planes.

We applied a machine learning method based on a Gaussian process optimization [46]. A Python code using the GPyOpt library [47] was used in the operation. The evaluation parameter was the radiation intensity measured by HgCdTe detectors. The parameters to change were the knobs listed earlier. Typically three or four knobs were used simultaneously in the optimization, and the best parameter set was found after approximately 50 epochs. Then the optimization continued using other knobs. In the first half, the optimization maximized the first undulator output, after which it was switched to the second undulator output. Figure 24 shows an example of the FEL power trend during the FEL optimization. Typically, it took approximately 4 h to establish maximum power at the second undulator.

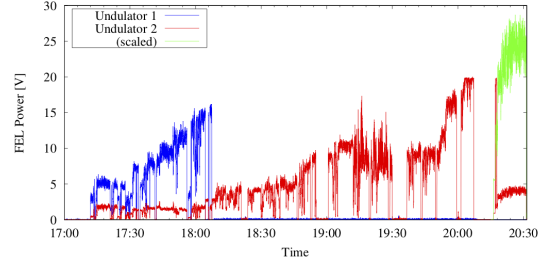


Figure 24: Trend of FEL power during the automatic tuning. Because the detector reached saturation (at 20:00), we changed the detector position longitudinally and continued the tuning. To correct the discontinuity of the detector signal, a scaled data (after 20:15) is also shown. The final absolute energy measurement was performed by switching to the pyrodetector.

After the FEL maximization tuning, we measured the chirp phase. Since the auto tuning procedure, especially the knobs of injector RF and main linac RF, can change the longitudinal energy chirp of the bunch. The final chirp phase at maximized FEL was measured to be  $+29^\circ$  for 1.3 GHz RF.

After we tuned the FEL output using auto-optimization, we measured the final beam parameters described in Sec. 4.1.1 and the responses of the knobs over a wide range to check their sensitivity. Figure 25 shows the FEL output response to the  $R_{56}$  knob. The FEL output of both undulators became maximum under the same condition. The FWHMs of the peaks were approximately 0.03 m in  $R_{56}$ .

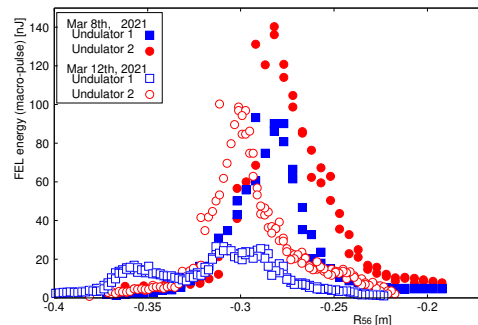


Figure 25: Response of FEL output power to the  $R_{56}$  knob. Two sets of measurements conducted on different days are shown. The FEL tuning procedure was repeated at the start of the beam operation on each day.

Figure 26 shows the FEL output response to the vertical and horizontal steering magnets upstream of the first undulator. The FWHMs of the peaks were approximately 0.4 mm (vertical) and 0.8 mm (horizontal) of the beam position offset at the undulator entrance.

#### 4.2. FEL characterization

Figure 27 shows the spatial profile of radiation at the second undulator measured by scanning the HgCdTe de-

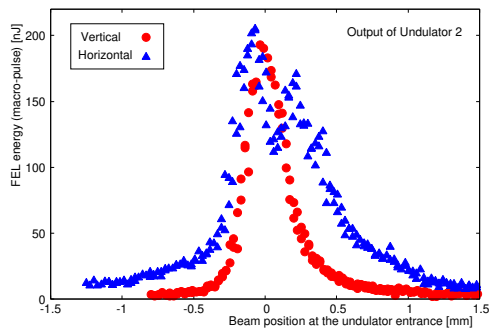


Figure 26: Response of FEL output power to the upstream steering magnet. Two sets of measurements, vertical and horizontal scans, are shown. The horizontal axis is the estimated beam position change at the entrance of the first undulator.

detector in two dimensions. By changing the longitudinal position, the spot size change around the focal position could be measured. The pyroelectric detector measurements were performed at the focal position.

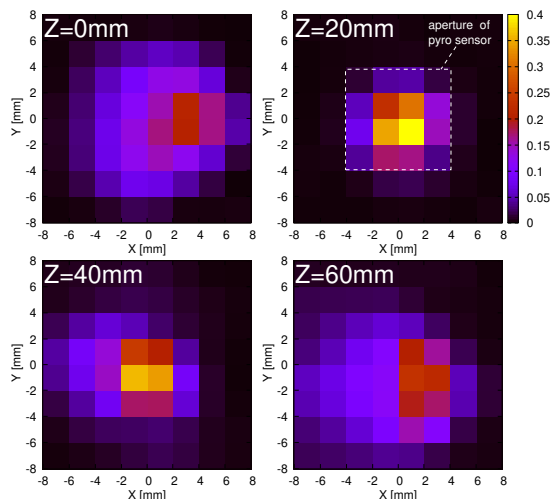


Figure 27: FEL spatial profiles at the second undulator output scanned around the focal point of the parabolic mirror.  $Z$  denotes the longitudinal position of the detector. It was confirmed that the spot size was minimum at  $Z = 20$  mm and was smaller than the aperture of the pyrosensor used for total energy measurement.

After the FEL optimization tuning, the absolute energy of the radiation was measured with the calibrated pyroelectric detector. Figure 28 shows the analog signal data when the maximum power was recorded. The BPF was inserted to measure the  $20 \mu\text{m}$  component. The detectors were calibrated as  $6.0 \text{ nJ/mV}$  at an infrared wavelength of  $976 \text{ nm}$ , and it becomes  $6.9 \text{ nJ/mV}$  at  $20 \mu\text{m}$  according to the absorption spectrum. Using this calibration, the energies directly measured at each detector were  $34.5 \text{ nJ/macro-pulse}$  and  $345 \text{ nJ/macro-pulse}$  for the first and second output port, respectively. To evaluate the orig-

inal energy at the undulator in vacuum, the following corrections should be applied: The reflectance of gold-plated mirrors—reflectance of each mirror was estimated as 0.95. The transmission of the BPF at a wavelength of  $20 \mu\text{m}$  was measured as 0.80. The transmission of the KRS-5 window was measured as 0.78. The geometrical efficiencies of hole mirror were estimated as 0.72 (first undulator) and 0.95 (second undulator), which were based on the simulation of the FEL radiation spatial profile. Including all these corrections, the energies at each undulator were  $94 \text{ nJ/macro-pulse}$  and  $753 \text{ nJ/macro-pulse}$ . Because each macro-pulse consisted of 130 bunches, it corresponded to  $0.72 \text{ nJ/bunch}$  and  $5.8 \text{ nJ/bunch}$ .

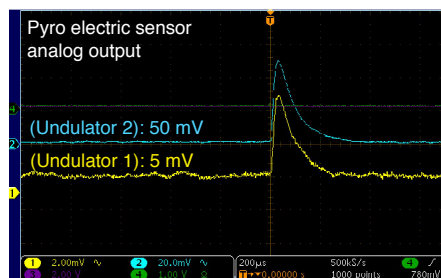


Figure 28: Absolute energy measurement of FEL macro-pulse. Analog signals of the amplifier of pyroelectric detectors were recorded. The peak voltage can be converted to the absolute energy using a calibration coefficient of  $6.9 \text{ nJ/mV}$  at  $20 \mu\text{m}$  wavelength.

Although a spectrometer system was not ready in this first commissioning, we measured the center wavelength of the radiation using a simple method. The ZnSe plate (Thorlabs, WG71050-E3) used as an attenuator was utilized as a standard sample that has a known transmission spectrum. By measuring the HgCdTe signal with and without the ZnSe plate, the transmission was measured. The BPF was off in this measurement. By repeating the measurement while changing the phase of both APU undulators simultaneously, we obtained the transmission curve in Fig. 29. The data were consistent with the specified transmission curve of the ZnSe plate (anti-reflective coating).

To show the stability of the FEL output, we measured the radiation intensity in a free run of 30 min. The measurement was performed with the HgCdTe detectors, and their absolute energy was calibrated by comparing with the pyrosensor just before the measurement. The shot-by-shot fluctuation was measured as 7% in RMS for both undulators. Note that a single shot of macro-pulse consists of 130 bunches. Assuming a non-correlated random Gaussian distribution, the bunch-by-bunch fluctuation is estimated as 80%.

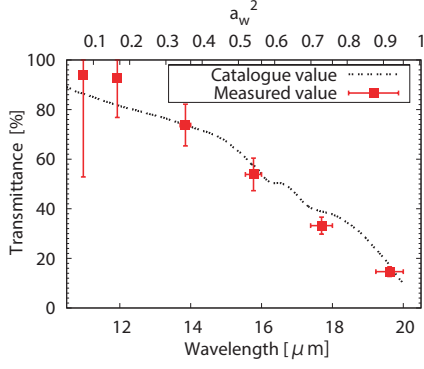


Figure 29: Transmission measurement of the ZnSe sample for showing wavelength tunability. The signal ratio of the HgCdTe detector between the conditions with and without the sample were measured while changing the undulator phase. Assuming the calculated wavelength change, the dependence was consistent with the transmission spectrum of the sample specified in the catalog.

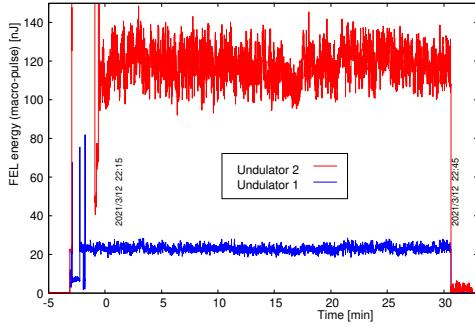


Figure 30: Trend of FEL energy in a free run of 30 min. Shot-by-shot voltage of the detectors was recorded continuously. (The beginning part of the data is for setting the detectors at non-saturated condition.)

#### 4.3. Characterization of Focused Laser Beam for Application Experiments

For the FEL application experiments, we sent the radiation to the irradiation setup. To confirm the spot size and its divergence, spatial profile measurements were performed at downstream of the telescope system. Figure 31 shows the results after the telescope tuning, adjustment of the distance between the parabolic mirror pair. Because the spot sizes at the two positions of 180 mm difference were measured to be the same, a collimated condition was established. The spot size injected to the irradiation system was estimated as 16.5 mm (horizontal)  $\times$  10.5 mm (vertical) in RMS size of the photon density distribution.

In the irradiation system, the spot size on the sample was measured by knife-edge scans. By scanning the knife edge on the radiation spot with a 200  $\mu\text{m}$  step while measuring the transmission energy, the spot size can be estimated. Figure 32 shows the estimated spot size as a function of the longitudinal position of the sample stage. The beam radius ( $2\sigma$ ) are plotted with the longitudinal position ( $z$ ) and fitted by an analytical Gaussian beam

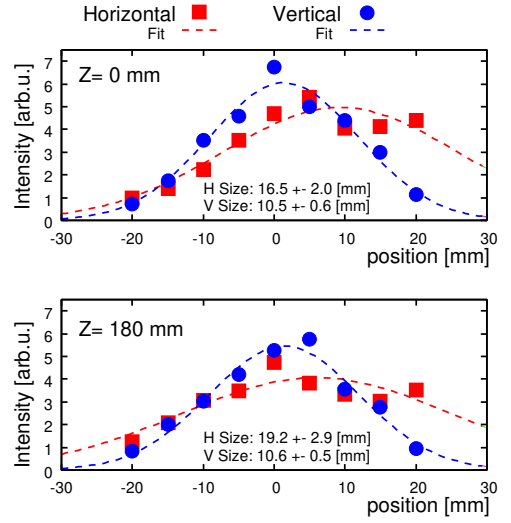


Figure 31: Results of FEL spatial profile measurements downstream of the telescope. Measurements were performed at two longitudinal positions, namely, at  $Z = 0$  and 180 mm. The projected distribution in two axes were fitted with a Gaussian function. Because the sizes were the same in the two positions, the telescope was well adjusted for converting the FEL to a collimated beam.

propagation equation to estimate beam quality factor  $M^2$  [48]. The minimum spot on the sample was  $0.345 \pm 0.040$  mm (2-RMS size,  $2\sigma_x$ ) in  $x$  direction. The 2-RMS size for  $y$  direction measured only one  $z$  position. The  $M^2$  was estimated as  $8.1 \pm 0.85$  for  $x$  direction. The measured macro-pulse energy ( $E$ ) was 207 nJ, due to clipping by the 25.4 mm aperture of the shutter and the parabola mirror. The peak fluence ( $Fp = 2E/(\pi(2\sigma_x)(2\sigma_y))$ ) is estimated as  $5.5 \times 10^{-5}$  J/cm<sup>2</sup> (for a macro-pulse) and  $0.42 \times 10^{-6}$  J/cm<sup>2</sup> (for a pulse) with the measured beam size of  $2\sigma_x = 385 \mu\text{m}$  and  $2\sigma_y = 625 \mu\text{m}$ . These information are indispensable for application experiments to quantitatively evaluate the effect of mid-infrared FEL irradiation on various material.

## 5. DISCUSSION

A demonstration experiment of mid-infrared SASE FEL targeting a wavelength of 20  $\mu\text{m}$  was performed at the cERL. In spite of the adverse circumstance that the beam quality was strongly affected by space charge effects, we developed a procedure to transport the beam in a controlled manner to the exit of the FEL layout. The procedure for FEL tuning has been established.

The FEL output energy was estimated as 5.8 nJ/pulse at 20  $\mu\text{m}$  wavelength at the exit of the second undulator. Comparing the extracted FEL energy with the beam energy of the 60 pC bunch at 17.7 MeV, which is approximately 1 mJ, the beam-to-radiation conversion efficiency is calculated as  $6 \times 10^{-6}$ . The obtained efficiency is rather lower than that naively expected with the Pierce parameter. One reason for the discrepancy is the slippage effect. According to a realistic three-dimensional simulation, the

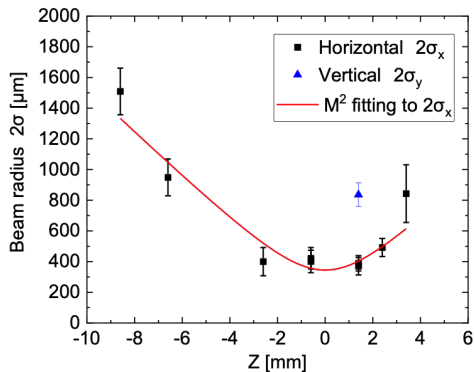


Figure 32: Spot size on the sample in the irradiation setup. The measurement was performed with a knife-edge scan. The data were fitted with a hyperbolic function to estimate the minimum size and beam quality ( $M^2$ ).

experimental results can be understood. In fact, the measured FEL energy was higher than that from the naive simulation shown in Fig. 3. The measured FEL energy at the exit of the first undulator was 0.72 nJ/bunch. It is about 10 times higher than the energy from the simulation. There appears to be an effect that enhances the start-up of the FEL process. We guess that there existed a fine structure that cannot be reproduced in the simulation input in the initial bunch density distribution. The coherent spontaneous emission (CSE) from the fine structure worked as a seed. The kinks that appeared in the longitudinal phase space distribution due to microbunching instability (MBI) as shown in Fig. 4 might have worked as the seed of the CSE. In the simulation, we can reproduce the effect by introducing an empirical parameter of 0.02% initial energy modulation.

The power gain in the second undulator with respect to the first undulator output was measured in the range of 5 to 10 after the final tuning. This is evidence of the contribution of the FEL to the amplification effect, which is not due to just the CSE. The amplification factor is consistent with the expectation from the simulation in Fig. 3. The strong dependence of the FEL output on the incoming beam position shown in Fig. 26 is another piece of evidence.

We performed beam tuning for FEL optimization approximately five times after the initial machine parameters in the operation period. The obtained FEL output power varied by approximately 20% in each trial on different days. In addition, the optimum  $R_{56}$  of the arc slightly changed as can be observed in Fig. 25. The repeatability of the machine was not too bad as the first commissioning.

In the burst mode beam operation, the beam energy changes in the macro-pulse due to the beam loading effect. The effect was estimated as 0.5% of the beam energy shift. Considering the resonance condition of the undulator, it changes the radiation wavelength by approximately 1%.

It is still much smaller than the relatively wide spectrum width shown in Fig. 5. However, because the FEL beam tuning is sensitive to the beam condition, the slight energy difference might affect the optimum condition of each bunch. To check the effect, we changed the macro-pulse width to 50%, that is from 130 bunches to 65 bunches. The FEL power then decreased to approximately 50%. This observation is evidence that most of the bunches in the macro-pulse contribute to the FEL output.

The undulator tapering scheme was applied to counteract the energy chirp in the bunch and enhance the FEL power. When we considered the undulator tapering in the design phase, we repeated the simulation, changing the tapering coefficient of the undulators. With the expected beam distribution used at the time, the simulation showed the FEL power enhancement by a factor of 5 as a result of setting the tapering coefficient to approximately  $-0.05$ . However, with the updated initial beam parameters in the actual beam operation, the response to the tapering has changed. To confirm whether undulator tapering worked, a reliable comparison experiment with and without tapering is necessary. Although it will be the subject of one of our forthcoming studies, it is outside the scope of this paper, which is about the first commissioning of the FEL.

The nominal FEL optimization was performed without using the chicane magnet. We tried turning on the chicane after the nominal FEL optimization. The FEL output showed some response to the current of the chicane magnet, i.e., the bump height. The enhancement effect due to the chicane is still under study and is outside the scope of this paper.

The radiation spectrum should be important for application experiments. Because of the limited beam time, we could not perform a detailed spectrum measurement. However, from the simple measurements of the ZnSe plate transmission in Fig. 29, we can state that the center wavelength is consistent with the expectation, and it can be adjusted by sliding the undulator. For a detailed study, we plan to install a spectrometer system in the next beam operation.

Beam profile measurement was carried out with the setup supposed for irradiation experiments. The knife edge measurement gives information on the focusing properties of FEL and the peak energy fluence on the sample. The estimated energy fluence ( $\sim 5.5 \times 10^{-5}$  J/cm<sup>2</sup> for one macro pulse) was smaller than the threshold fluence to achieve modification of resins [49]. Increase in the fluence by increasing the output energy and improvement of the beam quality together with tight focusing setup will realize various application experiments (laser processing, nonlinear phenomena) in near future.

To the best of our knowledge, this is the first experiment on an SASE FEL installed in an ERL-type accelerator layout. The most important advantage of the ERL layout is the possibility of handling a high average current beam. To investigate this possibility, the following studies will be necessary: Transport the beam to the main linac cavity

in the deceleration phase and safely guide it to the beam dump. For that, the efficiency of energy recovery should be optimized and the energy spread has to be managed in the momentum aperture of the beam dump line. The beam loss must be reduced to the allowable level determined by the shielding wall of the accelerator. The beam loss at the FEL hole mirrors and the narrow chamber of the undulator must be studied. We plan to extend the study to cover high-current operation in energy recovery mode. However, a discussion of this is outside the scope of this paper.

## 6. CONCLUSION

The FEL is one of the promising light sources in the mid-infrared range with wavelength tunability. Due to the slippage effects, the SASE FEL with a long undulator is not usually employed in the long wavelength range. On the other hand, the SASE FEL may have some advantages such as the possibility of single-pulse operation and the simplicity in establishing operating conditions, and most importantly, it is scalable to a future short-wavelength FEL.

We have constructed a mid-infrared SASE FEL setup in the layout of the cERL, which is a test accelerator of an ERL scheme. In spite of adverse circumstance of space charge effects due to the relatively low beam energy and long transport line, we have established a beam tuning procedure to transport the beam through the undulator and observed FEL emission at a wavelength of 20  $\mu\text{m}$ . A demonstration experiment of the FEL irradiation system was conducted successfully and confirmed the stable operation of the machine.

The results show that the layout of the cERL, a compact facility of the superconducting linac, has potential for use as a mid-infrared light source.

## Acknowledgments

We appreciate the cERL members for their support of the beam operation. This paper is based on results obtained from a NEDO Project Development of advanced laser processing with intelligence based on high-brightness and high-efficiency laser technologies (TACMI project). This work was partially supported by JSPS KAKENHI Grant Numbers 16H05991, 18H03473, and 15K04747. Construction of the cERL was supported by Photon and Quantum Basic Research Coordinated Development Program from the Ministry of Education, Culture, Sports, Science and Technology, Japan and by a Government (MEXT) Subsidy for Strengthening Nuclear Security.

## Appendix A. Space Charge Effects

The effect of the transverse space charge is not negligible at 17.5 MeV with a bunch charge of 60 pC. In a simple

model of envelope equation for a DC beam approximation [50, 51], the beam size development can be formalized as follows;

$$\sigma_x'' + K_x \sigma_x = \frac{I}{I_0(\beta\gamma)^3(\sigma_x + \sigma_y)} + \frac{\epsilon_x^2}{(\beta\gamma)^2 \sigma_x^3} \quad (\text{A.1})$$

and a similar equation can be formulated for the  $y$  direction.  $K_x$  denotes the external focusing by the magnets, and  $\epsilon_x$  is the normalized emittance.  $\sigma_x$  and  $\sigma_y$  are the horizontal and vertical beam sizes.  $I$  is the beam current, and  $I_0$  ( $\sim 17$  kA) is a constant.  $\beta$  is the normalized velocity, and  $\gamma$  is the Lorentz factor. From this equation, the defocusing force of the space charge can be rewritten as

$$K_{sc,x} = -\frac{I}{I_0(\beta\gamma)^3(\sigma_x + \sigma_y)\sigma_x} \quad (\text{A.2})$$

Comparing the integration of this effect distributed along a typical length of the beam line to the external focusing, we can understand that the effect is still small and can be treated as a perturbation for understanding the overall beam optics of our case.

Figure A.33 shows the calculated beam optics including the transverse space charge effect produced by the envelope equation and its comparison with the designed linear optics. Although the optics can seriously deviate from the design without any correction, it can be matched fairly well by interleaving matching tuning with an appropriate distance. Note that this model treats the space charge effect only linearly, and hence the emittance is conserved. However, nonlinear effect can dilute the beam emittance.

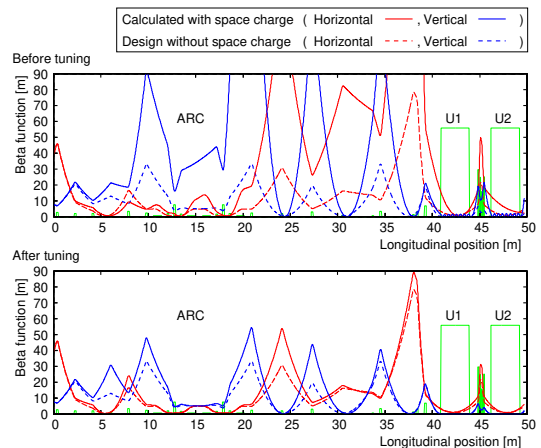


Figure A.33: Beam optics (beta function) from the exit of the main linac to the end of the FEL section calculated based on the envelope equation, including the transverse space charge effect. In the case of the magnet settings designed ignoring the space charge, the beta function deviates significantly from the design (top). After applying a local correction from upstream, the overall shape of the beta function agrees fairly well with the design (bottom).

Due to the longitudinal space charge (LSC) effect, the energy spread of the bunch increases in beam transport; i.e., the head part of the bunch is accelerated, and the tail

part is decelerated. The combination of the LSC effect with the bunch compression in the arc section severely disturbs the distribution in the longitudinal phase space [52]. Figure A.34 shows examples of the phase space distribution at the entrance of the FEL undulator calculated by elegant tracking. A complicated oscillation structure is formed in the arc section. This effect is called microbunching instability (MBI).

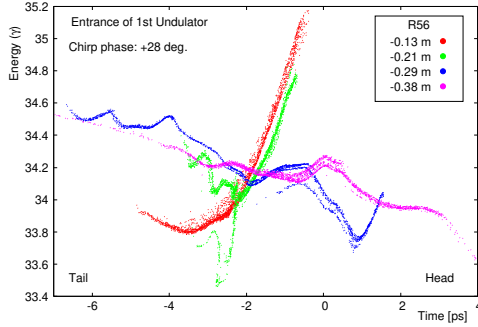


Figure A.34: Simulated longitudinal phase space distribution at the entrance of the FEL section. The distribution depends strongly on the bunch compression condition. Corresponding to the experimental condition, the chirp phase was set to be  $+28^\circ$ . Four cases of  $R_{56}$  are shown;  $R_{56} = -0.29$  m is the experimental case. Due to the LSC effect, the complicated shape appears especially in the overbunching cases.

## Appendix B. Undulator Tapering

Based on the beam transport simulations, we found that due to the space charge effect, the energy spread of the bunch at the entrance of the undulator became large, and it has a longitudinal energy chirp. To achieve an FEL gain throughout the undulator, the resonance condition of the FEL needs to be retained during the slippage over the full bunch length. To counteract the shift of the resonance condition due to the energy chirp, we utilized the undulator tapering scheme [53].

From the resonance condition of the undulator

$$\lambda = \frac{\lambda_u}{2\gamma^2}(1 + a_w^2) \quad , \quad (\text{B.1})$$

and considering the slice energy change  $\Delta\gamma$  and the undulator strength change  $\Delta a_w$  in one period of the undulator, the following relation is needed to keep the resonance condition in slip:

$$\frac{\partial\lambda}{\partial a_w} \Delta a_w = \frac{\partial\lambda}{\partial\gamma} \Delta\gamma \quad . \quad (\text{B.2})$$

This results in the following relation:

$$\frac{\Delta a_w}{\Delta\gamma} = \frac{1 + a_w^2}{\gamma a_w} \quad . \quad (\text{B.3})$$

The undulator tapering should be designed according to this relation.

Figure B.35 shows a simulation example demonstrating the effect of the tapering scheme. Even with a chirped beam, the FEL power can be recovered with an optimized tapered undulator to almost the same level as in the ideal case of an unchirped beam with a non-tapered undulator.

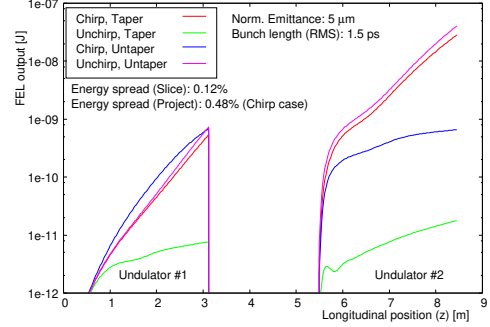


Figure B.35: Example simulation showing the effect of undulator tapering. Assuming a Gaussian distributed linearly chirped beam, development of FEL power along the undulator was calculated. Compared with the ideal case, unchirped beam with an untapered undulator, the power was limited in the chirped and untapered cases. The output power could be recovered to the ideal case by using tapered undulator.

## Appendix C. Orthogonal Combined Knob

To match the beam optics, namely four Twiss parameters, to the design at a position, at least four quadrupole magnets are necessary. The matching tuning is difficult and time consuming, involving repeating manual trials using one magnet at each step. To improve the efficiency of the beam tuning, we prepared orthogonal knobs by combined actions using four magnets simultaneously.

To define orthogonality, we used a complex representation of beam parameters. This is by analogy with the technique used in Gaussian beam optics of the laser beam [54], which has exactly the same mathematical structure. Using the  $\alpha$  and  $\beta$  of the Twiss parameters at the target position, the beam is represented as a point in the upper half area of the complex plane as

$$q = -\frac{\alpha\beta}{1 + \alpha^2} + \frac{\beta}{1 + \alpha^2}i \quad . \quad (\text{C.1})$$

We consider combined knobs that move the beam to the horizontal (real axis) or vertical (imaginary axis) direction in the plane. In the sense of two orthogonal directions, we call the knobs orthogonal. The real and imaginary motions can be understood as shifting the longitudinal position of the beam waist while maintaining the size of the waist and changing the size of the beam waist while maintaining the longitudinal position of the waist, respectively. Note that because the beam line components are represented as linear fractional transformations that preserve angles, the orthogonality is well defined in beam transport. The



orthogonal knobs were used in various cases in the beam tuning.

## References

- [1] I. Morichika, et al., Molecular ground-state dissociation in the condensed phase employing plasmonic field enhancement of chirped mid-infrared pulses, *Nature Comm.* 10 (2019) 3893. doi:10.1038/s41467-019-11902-6.
- [2] M. Först, et al., Nonlinear phononics as an ultrafast route to lattice control, *Nature Physics* 7 (2011) 854–856. doi:10.1038/nphys2055.
- [3] D. Maas, et al., Vibrational ladder climbing in NO by ultrashort infrared laser pulses, *Chem. Phys. Lett.* 270 (1997) 45–49. doi:10.1016/S0009-2614(97)00323-0.
- [4] Y. Ogi, et al., Vibrational excitation of CO molecules by infrared free electron laser, *Journal of Electron Spectroscopy and Related Phenomena* 128 (1) (2003) 67–73. doi:10.1016/S0368-2048(02)00211-6.
- [5] M. Toriumi, et al., Wavelength dependence of poly(p-hydroxystyrene) ablation by mid-infrared free-electron laser, *Journal of Photopolymer Science and Technology* 32 (2) (2019) 189–193. doi:10.2494/photopolymer.32.189.
- [6] P. Salén, et al., Matter manipulation with extreme terahertz light: Progress in the enabling THz technology, *Phys. Reports* 836-837 (2019) 1–74. doi:10.1016/j.physrep.2019.09.002.
- [7] C. Patel, Continuous-wave laser action on vibrational-rotational transitions of CO<sub>2</sub>, *Phys. Rev.* 136 (1964) A1187.
- [8] B. Schwarz, et al., Watt-level continuous-wave emission from a bifunctional quantum cascade laser/detector, *ACS Photonics* 4 (2017) 1225–1231. doi:10.1021/acsp Photonics.7b00133.
- [9] M. Maday, Stimulated emission of bremsstrahlung in a periodic magnetic field, *Journal of Applied Physics* 42 (1971) 1906. doi:10.1063/1.1660466.
- [10] D. Deacon, et al., First operation of a free-electron laser, *Phys. Rev. Lett.* 38 (1977) 892. doi:10.1103/PhysRevLett.38.892.
- [11] J. Ortega, et al., Extension in far-infrared of the CLIO free-electron laser, *Infrared Phys. Technol.* 49 (2006) 133–138. doi:10.1016/j.infrared.2006.01.011.
- [12] D. Oepts, et al., The free-electron-laser user facility FELIX, *Infrared Phys. Technol.* 36 (1995) 297–308. doi:10.1016/1350-4495(94)00074-U.
- [13] U. Lehnert, et al., Optical beam properties and performance of the MID-IR FEL at ELBE, in: *Proceedings of FEL Conference 2005*, 2005, pp. 286–287.
- [14] H. Kuroda, Status of the FEL-SUT project, *Japan J. Appl. Phys.* 41 (S1) (2002) 1–9. doi:10.7567/JJAPS.41S1.1.
- [15] O. A. Shevchenko, et al., The Novosibirsk free electron laser facility, in: *AIP Conference Proceedings*, Vol. 2299, 2020, p. 020001. doi:10.1063/5.0031513.
- [16] H. Zen, et al., High-extraction-efficiency operation of a mid-infrared free electron laser enabled by dynamic cavity desynchronization, *Phys. Rev. Accel. Beams* 23 (2020) 070701. doi:10.1103/PhysRevAccelBeams.23.070701.
- [17] J. Kaminski, et al., Far-infrared cavity dump coupling of the UC Santa Barbara free-electron laser, *Appl. Phys. Lett.* 57 (1990) 2770. doi:10.1063/1.103782.
- [18] N. Nishimori, et al., Operational experience of a 500 kV photoemission gun, *Phys. Rev. Accel. Beams* 22 (2019) 053452. doi:10.1103/PhysRevAccelBeams.22.053402.
- [19] S. Okuda, et al., Self-amplified spontaneous emission at wavelength of 20 and 40  $\mu\text{m}$  from single-bunch electron beams, *Nucl. Instrum. Meth. A* 331 (1993) 76–78. doi:10.1016/0168-9002(93)90017-C.
- [20] D. Bocek, et al., Observation of sase at 47  $\mu\text{m}$ , *Nucl. Instrum. Meth. A* 375 (1996) 13–16. doi:10.1016/0168-9002(95)01361-X.
- [21] R. Prazeres, et al., Observation of self-amplification spontaneous emission in the mid-infrared in a free-electron laser, *Phys. Rev. Lett.* 78 (1997) 2124. doi:10.1103/PhysRevLett.78.2124.
- [22] M. Hogan, et al., Measurements of high gain and intensity fluctuations in a self-amplified, spontaneous-emission free-electron laser, *Phys. Rev. Lett.* 80 (1998) 289. doi:10.1103/PhysRevLett.80.289.
- [23] D. Nguyen, et al., Self-amplified spontaneous emission driven by a high-brightness electron beam, *Phys. Rev. Lett.* 81 (1998) 810. doi:10.1103/PhysRevLett.81.810.
- [24] E.L.Saldin, et al., Self-amplified spontaneous emission fel with energy-chirped electron beam and its application for generation of attosecond x-ray pulses, *Phys. Rev. ST-AB* 9 (2006) 050702. doi:10.1103/PhysRevSTAB.9.050702.
- [25] Y. Ding, et al., Generation of attosecond x-ray pulses with a multi cycle two-color enhanced self-amplified spontaneous emission schem, *Phys. Rev. ST-AB* 12 (2009) 060703. doi:10.1103/PhysRevSTAB.12.060703.
- [26] W.M.Fawley, Production of ultrashort FEL XUV pulses via a reverse undulatory taper, *Nucl. Instrum. Meth. A* 593 (2008) 111–115. doi:10.1016/j.nima.2008.04.051.
- [27] J. Duris, et al., Superradiant amplification in a chirped-tapered x-ray free-electron laser, *Phys. Rev. Accel. Beams* 23 (2020) 020702. doi:10.1103/PhysRevAccelBeams.23.020702.
- [28] M. Akemoto, et al., Construction and commissioning of the compact energy-recovery linac at KEK, *Nucl. Instrum. Meth. A* 877 (2018) 197–219. doi:10.1016/j.nima.2017.08.051.
- [29] I. Ben-Zvi, Superconducting energy recovery linacs, *Supercond. Sci. Technol.* 29 (2016) 103002.
- [30] S. Benson, et al., First lasing of the jefferson lab ir demo fel, *Nucl. Instrum. Meth. A* 429 (1) (1999) 27–32. doi:10.1016/S0168-9002(99)00061-3.
- [31] R. Hajima, et al., First demonstration of energy-recovery operation in the JAERI superconducting linac for a high-power free-electron laser, *Nucl. Instrum. Meth. A* 507 (1) (2003) 115–119. doi:10.1016/S0168-9002(03)00849-0.
- [32] F. Jackson, D. Angal-Kalinin, Y. M. Saveliev, P. H. Williams, A. Wolski, Longitudinal transport measurements in an energy recovery accelerator with triple bend achromat arcs, *Phys. Rev. Accel. Beams* 19 (2016) 120701. doi:10.1103/PhysRevAccelBeams.19.120701.
- [33] M. Arnold, J. Birkhan, J. Pforr, N. Pietralla, F. Schließmann, M. Steinhorst, F. Hug, First operation of the superconducting Darmstadt linear electron accelerator as an energy recovery linac, *Phys. Rev. Accel. Beams* 23 (2020) 020101. doi:10.1103/PhysRevAccelBeams.23.020101.
- [34] Y. Socol, G. N. Kulipanov, A. N. Matveenko, O. A. Shevchenko, N. A. Vinokurov, Compact 13.5-nm free-electron laser for extreme ultraviolet lithography, *Phys. Rev. ST Accel. Beams* 14 (2011) 040702. doi:10.1103/PhysRevSTAB.14.040702.
- [35] R. Bonifacio, et al., Physics of the high-gain fel and superradiance, *Rivista Del Nuovo Cimento* 13 (9) (1990) 1–69.
- [36] *General Particle Tracer, Pulser Physics, Flamingostraat 24, 3582 SX Utrecht, The Netherlands.*
- [37] M. Borland, A flexible sdds-compliant code for accelerator simulation, in: *ICAP(00)*, ACM Press, Darmstadt, Germany, 2000, pp. 417–426. doi:10.2172/761286.
- [38] S. Reiche, Genesis 1.3: a fully 3d time-dependent fel simulation code, *Nucl. Instrum. Meth. A* 429 (1999) 243. doi:10.1016/S0168-9002(99)00114-X.
- [39] T. Akagi, et al., Narrow-band photon beam via laser Compton scattering in an energy recovery linac, *Phys. Rev. Accel. Beams* 19 (2016) 114701. doi:10.1103/PhysRevAccelBeams.19.114701.
- [40] Y. Honda, et al., Stimulated excitation of an optical cavity by a multibunch electron beam via coherent-diffraction-radiation process, *Phys. Rev. Lett.* 121 (2018) 184801. doi:10.1103/PhysRevLett.121.184801.
- [41] M. Shimada, et al., in preparation.
- [42] G. Penco, et al., Experimental demonstration of enhanced self-amplified spontaneous emission by an optical klystron, *Phys. Rev. Lett.* 114 (2015) 013901. doi:10.1103/PhysRevLett.114.013901.
- [43] R. Carr, Adjustable phase insertion devices as x-ray sources,

- Nucl. Instrum. Meth. A 306 (1991) 391–396. doi:10.1016/0168-9002(91)90346-R.
- [44] D. Skinner, R. Whitcher, Measurement of the radius of a high-power laser beam near the focus of a lens, *J. Phys. E Scientific Instruments* 5 (3) (1972) 237.
- [45] Y. Honda, et al., Beam tuning and bunch length measurement in the bunch compression operation at the cERL, *Nucl. Instrum. Meth. A* 875 (2017) 156–164. doi:10.1016/j.nima.2017.09.027.
- [46] J. Duris, et al., Bayesian optimization of a free-electron laser, *Phys. Rev. Lett.* 124 (2020) 124801. doi:10.1103/PhysRevLett.124.124801.
- [47] GPyOpt, <https://sheffieldml.github.io/GPyOpt/>.
- [48] ISO Central Secretary, “lasers and laser-related equipment - test methods for laser beam widths, divergence angles and beam propagation ratios”, Standard, International Organization for Standardization (2005).
- [49] T. Sato, et al., Laser processing of polymeric materials by quantum cascade lasers (conference presentation), in: *Proc. SPIE 11267, Laser Applications in Microelectronic and Optoelectronic Manufacturing (LAMOM) XXV*, Vol. 11267, 2020. doi:10.1117/12.2551053.
- [50] J. L. Sarafini, Envelope analysis of intense relativistic quasilaminar beams in rf photoinjectors: A theory of emittance compensation, *Phys. Rev. E* 55 (1997) 7565. doi:10.1103/PhysRevE.55.7565.
- [51] S. Anderson, et al., Space-charge effects in high brightness electron beam emittance measurements, *Phys. Rev. ST-AB* 5 (2002) 014201. doi:10.1103/PhysRevSTAB.5.014201.
- [52] Z. Huang, et al., Suppression of microbunching instability in the linac coherent light source, *Phys. Rev. ST-AB* 7 (2004) 074401. doi:10.1103/PhysRevSTAB.7.074401.
- [53] L. Gianessi, et al., Self-amplified spontaneous emission free-electron laser with an energy chirped electron beam and undulator tapering, *Phys. Rev. Lett.* 106 (2011) 144801. doi:10.1103/PhysRevLett.106.144801.
- [54] A. Yariv, *Photonics: Optical Electronics in Modern Communications* (6th edition), Oxford university press, 2006.